David A. Mills, Daniel Blood, and Mark Sheplak. "Characterization of a sapphire optical wall shear stress sensor for high-temperature applications", 54th AIAA Aerospace Sciences Meeting, AIAA SciTech Forum, (AIAA 2016-2016), https://doi.org/10.2514/6.2016-2016

Characterization of a Sapphire Optical Wall Shear Stress Sensor for High-Temperature Applications

David A. Mills*, Daniel Blood†, and Mark Sheplak‡

Interdisciplinary Microsystems Group, University of Florida, Gainesville, FL, 32611, USA

This paper presents the development and initial experimental characterization of the first sapphire micromachined wall shear stress sensor for high-temperature applications utilizing geometric moiré optical transduction. The microelectromechanical systems (MEMS) sensor utilizes a folded tether floating element structure to extend the operating range of the sensor. Picosecond pulsed laser micromachining is employed to pattern mechanical structures in sapphire, and a four-channel alumina fiber array with sapphire optical fibers is used to interrogate the moiré fringe. Platinum thin-film gratings and a stainless steel package enable a theoretical maximum operating temperature in excess of $800°C$**. Calibration of the sensor system in differential mode demonstrates a dynamic shear stress sensitivity of** $76.8\ \mu V/Pa$ **at** $1.128\ kHz$**, sensor resonance of** $3.5\ kHz$**, pressure rejection ratio of** $75\ dB$**, minimum detectable shear stress of** $4.6\ mPa$ **at** $1.128\ kHz$ **for a** $1\ Hz$ **bin, and an experimentally verified dynamic range of** $52\ dB$**.**

Nomenclature

a	Duct half-height
A_t	Area, tether cross-section
c	Isentropic speed of sound
C_{me}	Lumped mechanical compliance
d_s	Sensor location relative to end wall
E	Elastic modulus
f_{res}	Resonant frequency
G	Moiré fringe period
g_1	Movable grating pitch
g_2	Fixed grating pitch
H_p	Pressure rejection ratio
k	Acoustic wavenumber
I_y	Area moment of inertia
L_e	Floating element length
L_t	Tether length
L_{tr}	Truss length
$M_{element}$	Floating element mass
M_{me}	Lumped mechanical mass, total
M_{tme}	Lumped mechanical mass, single folded tether
$M_{t1,me}$	Lumped mechanical mass, fixed beam
$M_{t2,me}$	Lumped mechanical mass, truss
$M_{tr,me}$	Lumped mechanical mass, guided beam
P	Pressure

*Post-Doctoral Associate, Department of Electrical and Computer Engineering, 946 Center Dr, Gainesville, FL, 32611, AIAA Member.

†Assistant Professor, Department of Mechanical Engineering, Valparaiso University, Valparaiso, IN, 46383.

‡Professor, Department of Electrical and Computer Engineering, 968 Center Dr, Gainesville, FL, 32611, AIAA Associate Fellow.

p'	Dynamic pressure
R	Reflection coefficient
S	Dynamic shear stress sensitivity
S_p	Dynamic pressure sensitivity
T	Floating element and folded tether thickness
$V_{0,n}$	Output voltage
W_e	Floating element width
W_t	Tether width, top
$W_{t,b}$	Tether width, bottom
W_{tr}	Truss width
α	Grating angular misalignment
δ	Floating element displacement
ν	Kinematic viscosity
ρ	Density
τ_w	Wall shear stress
ϕ	Moiré fringe phase
ω	Angular frequency

I. Introduction

The ability to accurately quantify wall shear stress in high-temperature, harsh environments is important for multiple research and industrial communities. In the aerospace research community, measurement of skin friction within fundamental flows such as compressible zero pressure gradient boundary layers can lead to improved turbulence models. The study of more complex flow phenomena such as laminar to turbulent boundary layer transition, shock-wave/boundary layer interactions, and separated flows can lead to improved performance in hypersonic flight vehicles. Active flow control for high-performance gas turbines and flight vehicles can be implemented in conjunction with skin friction measurement to delay flow separation and reduce viscous drag.[1] Outside of the aerospace community, measurement of fluid properties within extruders and other high-temperature liquid environments present challenges for traditional shear stress measurement techniques.

Direct wall shear stress measurement is typically accomplished via a force balance in which a movable floating element deflects due to an integrated shear force. For an open loop system this floating element is attached to a compliant structure which resists the deflection and provides a restorative force for returning the floating element to its nominal position. An example of such a structure is shown in Figure 1, with the four tethers shown in the top view providing an effective spring constant for the sensor. Winter provides numerous examples of macroscale force balance sensors for skin friction measurement; however, these sensors often suffer from cross-axis sensitivity to pressure gradients, accelerations, and vibrations and poor temporal resolution due to the mass of the structure, a compromise between spatial resolution and small force detection, and errors induced by flow disturbances such as gaps, steps, and misalignment of the sensor.[2,3] In order to mitigate these performance issues, simple scaling analyses show that a reduction in sensor size by using MEMS-based floating element sensors improve temporal and spatial resolution and also reduce the sensitivity to cross-axis inputs as well as gap and misalignment effects.[4,5]

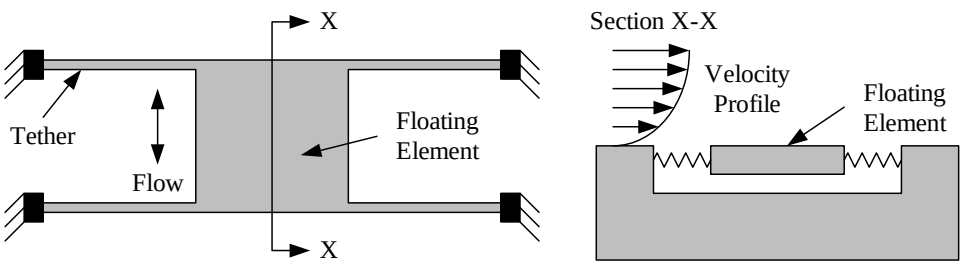

Figure 1. Simplified views of a generic floating element shear stress sensor structure (adapted from Naughton and Sheplak[4]).

Capacitive,[6–11] optical,[12–14] and piezoresistive[15–18] sensing methods have all been implemented the development of silicon-based direct wall shear stress sensors; however, the application of these sensors in real-world test facilities has proven difficult. Furthermore, use of these sensors is limited to $\sim 500°C$ because of plastic deformation above these temperatures.[19] In addition to silicon, previous research efforts in the development of high-temperature microfabricated transducers have focused on the use of silicon carbide,[20–22] diamond,[23,24] and sapphire,[25,26] among other materials. The majority of these sensors, however, are either piezoresistive or capacitive which limits their high-temperature capabilities due to the need for electronics in close proximity to the sensor. Tiliakos et al.[22] demonstrated the survivability of a silicon carbide capacitive floating element shear stress sensor in a Mach 5 flow for $45 - 90$ *sec* with estimated shear stress levels of $500 - 700$ Pa and total temperatures near $700°C$; however, no measured shear stress data was presented for the sensor.

Fiber-optic sensors provide several advantages over these traditional sensing methods in harsh environments with temperatures in excess of $500°C$, including being a passive sensing method, immune to electromagnetic interference, and nonconductive. These qualities are further enhanced via the use of sapphire because of its operating temperature range and high resistance to erosive and corrosive environments. This research leverages previous efforts in the development of a silicon-on-Pyrex optical wall shear stress sensor[13,14,27,28] by employing a similar transduction method that utilizes geometric moiré fringe formation and quadrature phase estimation to determine the wall shear stress. The operating temperature range of the sensor is extended beyond that of silicon-based sensors via the use of sapphire for the sensor structure and high-temperature optical fiber array. Section II provides and overview of the wall shear stress sensor including the optical transduction method, mechanical sensor design, and high-temperature packaging. The experimental setup and results for dynamic calibration are presented in Sections III and IV, respectively, followed by a summary of the results and planned future work in Section V.

II. The Sapphire Optical Wall Shear Stress Sensor

This section provides an overview of the sapphire optical shear stress sensor, with an illustration of the basic sensor structure shown in Figure 2. The use of sapphire substrates and optical fibers extends the high-temperature limit beyond that of silicon; however, traditional silicon microfabrication technologies are largely inapplicable due to the high hardness and chemical inertness of sapphire, requiring novel fabrication processes for patterning of the floating element and other features. The fundamentals of moiré fringe formation and interrogation are first presented, followed by details of the sensor design and packaging of the sensor and sapphire optical fiber array.

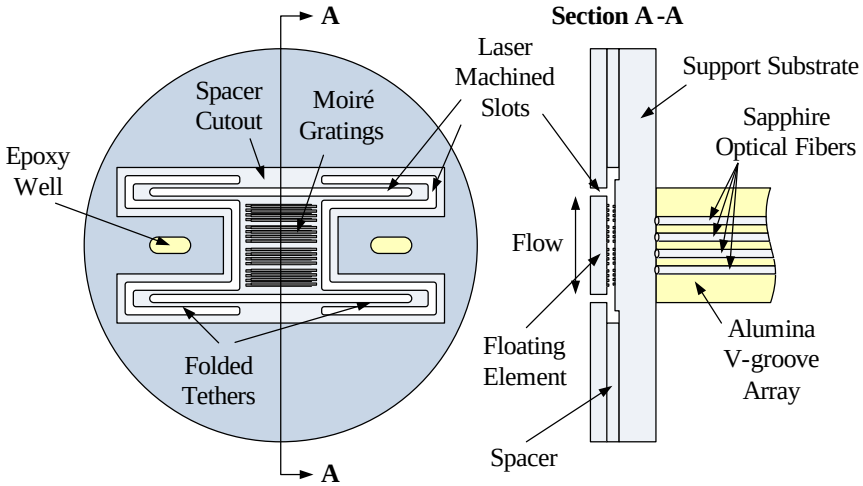

Figure 2. Illustration of the sapphire optical wall shear stress sensor.

II.A. Moiré Fringe Formation and Interrogation

The method of moiré fringe pattern formation and interrogation is the same as that utilized previously by Mills et al.,[28,29] utilizing two sets of platinum bar and space gratings aligned parallel to one another. From Mills et al.,[27] assuming pure translation of the entire movable grating, the moiré fringe period G for a movable grating of pitch g_1 and a fixed grating of pitch g_2 is

$$\frac{1}{G} = \frac{1}{g_1} - \frac{\cos\alpha}{g_2}, \tag{1}$$

where α represents a fixed angular misalignment. This effect is shown Figure 3, where the reflected intensity is represented by a triangle wave with a dc offset.

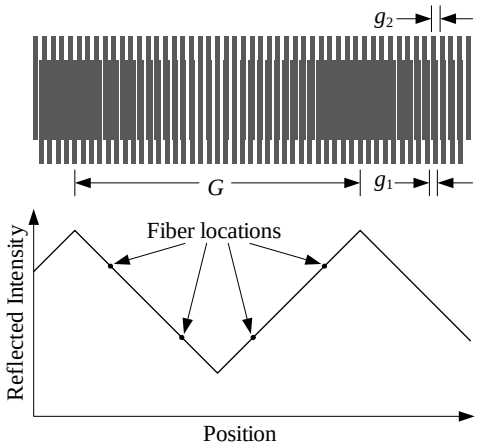

Figure 3. Illustration of the fiber locations for quadrature method of estimating the moiré fringe phase. Reprinted from Mills et al.[29]

The quadrature phase estimation method previously utilized for a silicon-on-Pyrex sensor by Mills et al.[28] is again used, reducing sensitivity to pressure fluctuations and source drift while also minimizing cross-talk between fibers. The phase of the moiré fringe is estimated using the expression

$$\phi = \tan^{-1}\left(\frac{V_{0,3} - V_{0,1}}{V_{0,4} - V_{0,2}}\right), \tag{2}$$

where $V_{0,n}$ is the output voltage of the n^{th} channel. Because only four positions along the moiré fringe are required to perform the quadrature phase estimate, discrete points are selected at 90° intervals and the grating overlap is duplicated to cover the entire fiber area. This provides an area of constant grating overlap (either 25% or 75%) for each fiber as shown in Figure 4 which relaxes alignment tolerances between the sensor and fiber array during packaging.

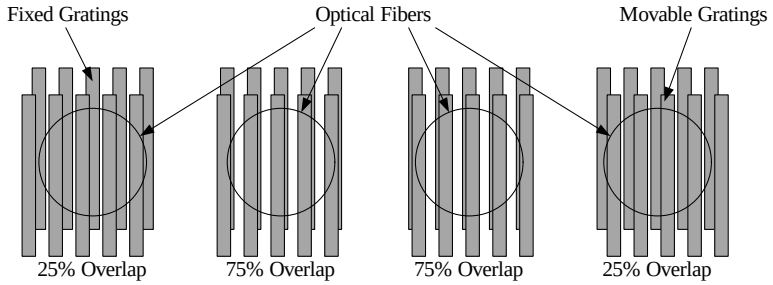

Figure 4. Illustration of the constant grating overlap for each discrete fiber location on the moiré fringe.

II.B. Sensor Design

The wall shear stress sensor shown in Figure 2 consists of a floating element substrate, a support substrate, and a thin spacer. All of the patterned features in these substrates were created using picosecond pulsed

laser micromachining.[30] The spacer is used to create a controlled 25 μm gap between the floating element and support substrates while maintaining optical quality in the areas where the gratings are patterned. The moiré fringe segments are created by patterning a platinum thin film on both the floating element and support substrate. Additional fabrication details for the sensor can be found in Ref. 29.

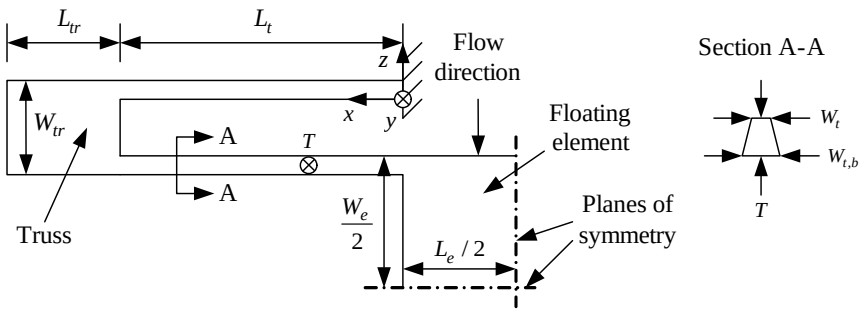

Figure 5. Quarter sensor model used for mechanical design of the folded tether floating element shear stress sensor structure.

The floating element of thickness T with length L_e and width W_e is suspended over a cavity by four folded tethers that provide the restorative force to counteract the integrated shear force exerted on the floating element. The folded tether design prevents buckling due to thermal expansion at high temperatures and also expands the linear deflection range of the sensor compared to straight tether designs. The static deflection δ of the sensor due to an applied wall shear stress τ_w is determined using a quarter sensor model as shown in Figure 5. It is assumed that the truss section remains rigid which creates compatibility conditions relating the deflection and slope of the two tether sections of width W_t and length L_t. Using Euler-Bernoulli beam theory for each section of the tether structure to determine the total deflection at the floating element, the deflection is

$$\delta = \tau_w \frac{W_e L_e L_t^3}{24 E I_y} \left(1 + 4\frac{W_t L_t}{W_e L_e} + 2\frac{W_{tr} L_{tr}}{W_e L_e}\right), \tag{3}$$

where E is the elastic modulus of sapphire and I_y is the area moment of inertia of the tether cross-section. Due to sidewall taper in the laser machined features, a trapezoidal tether cross-section with top width W_t and bottom width $W_{t,b}$ is used. The result is an expression comprised of the deflection due to an integrated shear force acting on the floating element[31] plus additional terms that account for the shear force acting on the tethers and truss sections.

An estimate of the resonant frequency of the floating element structure is obtained using the expression

$$f_{res} = \frac{1}{2\pi}\sqrt{\frac{1}{C_{me} M_{me}}}, \tag{4}$$

where C_{me} and M_{me} are the lumped mechanical compliance and mass of the sensor, respectively, determined using the method described in Ref. 32. The floating element and truss sections are considered rigid bodies; therefore, the compliance is determined by equating the potential energy stored within the four pairs of tethers to an effective compliance lumped at the floating element, given here as

$$C_{me} = \frac{\frac{L_t^3}{24 E I_y}\left(1 + 4\frac{W_t L_t}{W_e L_e} + 2\frac{W_{tr} L_{tr}}{W_e L_e}\right)^2}{\left[\begin{array}{c} 1 + 8\frac{W_t L_t}{W_e L_e} + 4\frac{W_{tr} L_{tr}}{W_e L_e} + \frac{128}{5}\left(\frac{W_t L_t}{W_e L_e}\right)^2 + 20\left(\frac{W_{tr} L_{tr}}{W_e L_e}\right)^2 \\ +40\left(\frac{W_t L_t}{W_e L_e}\right)\left(\frac{W_{tr} L_{tr}}{W_e L_e}\right) + 8\left(\frac{W_t L_t}{W_e L_e}\right)\left(\frac{W_{tr} L_{tr}}{W_e L_e}\right)\left(\frac{L_{tr}}{L_t}\right) + 12\left(\frac{W_{tr} L_{tr}}{W_e L_e}\right)^2\left(\frac{L_{tr}}{L_t}\right) \end{array}\right]}. \tag{5}$$

Similarly, the effective mass of the four folded tethers lumped at the floating element is determined by equating the total kinetic energy of the folded tethers to the equivalent kinetic energy of the lumped system. The total lumped mass of the floating element structure is the sum of the effective mass of the four folded tethers M_{tme} plus the floating element mass $M_{element}$ and is given as

$$M_{me} = 4M_{tme} + M_{element} = 4M_{tme} + \rho W_e L_e T. \tag{6}$$

In Equation 6,

$$M_{tme} = M_{t1,me} + M_{tr,me} + M_{t2,me}, \tag{7}$$

where $M_{t1,me}$ $M_{tr,me}$, and $M_{t2,me}$ are the equivalent mass of the fixed beam, truss, and guided beam, respectively. The equivalent mass of each term in Equation 7 is determined individually and summed to give the equivalent mass of a single folded tether lumped at the floating element, given here as

$$\begin{aligned} M_{tme} = {} & 2\rho A_t L_t \frac{\left(\begin{array}{c} \frac{12}{35} + \frac{138}{35}\frac{W_t L_t}{W_e L_e} + \frac{201}{70}\frac{W_{tr} L_{tr}}{W_e L_e} + \left(\frac{W_{tr} L_{tr}}{W_e L_e}\right)\left(\frac{L_{tr}}{L_t}\right) + \frac{3968}{315}\left(\frac{W_t L_t}{W_e L_e}\right)^2 \\ + \frac{57}{7}\left(\frac{W_{tr} L_{tr}}{W_e L_e}\right)^2 + \frac{277}{14}\left(\frac{W_t L_t}{W_e L_e}\right)\left(\frac{W_{tr} L_{tr}}{W_e L_e}\right) + \frac{36}{5}\left(\frac{W_{tr} L_{tr}}{W_e L_e}\right)^2\left(\frac{L_{tr}}{L_t}\right) \\ + \frac{282}{35}\left(\frac{W_t L_t}{W_e L_e}\right)\left(\frac{W_{tr} L_{tr}}{W_e L_e}\right)\left(\frac{L_{tr}}{L_t}\right) + \frac{9}{5}\left(\frac{W_{tr} L_{tr}}{W_e L_e}\right)^2\left(\frac{L_{tr}}{L_t}\right)^2 \end{array} \right)}{\left(1 + 4\frac{W_t L_t}{W_e L_e} + 2\frac{W_{tr} L_{tr}}{W_e L_e}\right)^2} \\ & + \rho W_{tr} L_{tr} T \frac{\left(\begin{array}{c} \frac{1}{3}\left(\frac{L_{tr}}{L_t}\right)^2\left[4\frac{W_t L_t}{W_e L_e} + 6\frac{W_{tr} L_{tr}}{W_e L_e}\left(1 + \frac{L_{tr}}{L_t}\right)\right]^2 \\ + \frac{L_{tr}}{L_t}\left[4\frac{W_t L_t}{W_e L_e} + 6\frac{W_{tr} L_{tr}}{W_e L_e}\left(1 + \frac{L_{tr}}{L_t}\right)\right]\left[\frac{1}{2} + 5\left(\frac{W_t L_t}{W_e L_e} + \frac{W_{tr} L_{tr}}{W_e L_e}\right) + 3\frac{W_{tr} L_{tr}}{W_e L_e}\left(\frac{L_{tr}}{L_t}\right)^2\right] \\ + \left[\frac{1}{2} + 5\left(\frac{W_t L_t}{W_e L_e} + \frac{W_{tr} L_{tr}}{W_e L_e}\right) + 3\frac{W_{tr} L_{tr}}{W_e L_e}\left(\frac{L_{tr}}{L_t}\right)^2\right]^2 \end{array} \right)}{\left(1 + 4\frac{W_t L_t}{W_e L_e} + 2\frac{W_{tr} L_{tr}}{W_e L_e}\right)^2} \end{aligned}. \tag{8}$$

Equation 8 is then simply substituted into Equation 6 to determine the total lumped mass of the floating element structure. The physical dimensions, mechanical sensitivity, and resonant frequency for the selected floating element design are listed in Table 1.

Table 1. Geometry and performance characteristics for the sapphire optical shear stress sensor.

Parameter	Value	
Floating element length, L_e	2	mm
Floating element width, W_e	2	mm
Thickness, T	127	μm
Tether length, L_t	2	mm
Top tether width, W_t	42	μm
Bottom tether width, $W_{t,b}$	70	μm
Truss length, L_{tr}	150	μm
Truss width, W_{tr}	150	μm
Mechanical sensitivity, δ/τ_w	1.8	nm/Pa
Resonant frequency, f_{res}	5.35	kHz

II.C. Packaging

The complete shear stress sensor system requires a package for the sapphire sensor die and fiber array as well as optoelectronics to transmit light to and from the sensor and convert the reflected light to an output voltage to estimate the moiré fringe phase using Equation 2. The overall configuration of the sensor system including the optoelectronics, illustrated in Figure 6, is the same as that used by Mills et al.[28] for dynamic calibration of a silicon-on-Pyrex optical shear stress sensor. Over the frequencies tested, the photodiode array provides a low noise floor and high photoelectric sensitivity ($\sim 8 \times 10^5$ V/W) without requiring reverse biasing of the photodiodes. Uncertainty due to fluctuations in the optical source is minimized by using a single Appointech SD-series 850 nm LED housed in a fiber-coupled (FC) receptacle with a 200 μW nominal optical output connected directly to a Newport 850 nm 1x4 multimode fiber optic coupler.

The high-temperature fiber array utilizes four 120 μm diameter sapphire optical fibers placed in a laser machined alumina v-groove array to minimize thermal stresses between the sensor and fiber array. The v-groove array is similar to commercially available silicon arrays with 250 μm spacing between fibers. Cotronics 989F ceramic epoxy is used to secure the fibers within the array, and polishing of the ends of the array was performed by commercial vendors. The fiber diameter was chosen to enable the use of a standard multiple-fiber push-on (MPO) connector on the distal end of the array, creating a single robust connection to the low-temperature silica fiber couplers.

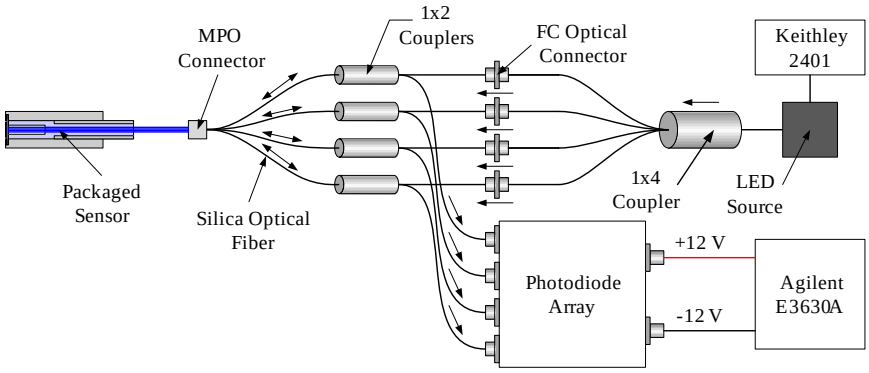

Figure 6. Schematic of the complete optoelectronic layout for the shear stress sensor. Arrows indicate the direction of light propagation (adapted from Mills et al.[28]).

Use of the shear stress sensor in high-temperature, high-speed flows requires that the package for the device be small, robust, and hydraulically smooth.[4] The optical transduction technique selected enables a simple package composed of the sensor, sapphire fiber array, and stainless steel housing and fiber conduit as shown in Figure 7. The sensor housing itself is 0.375 in in diameter and 1 in long, allowing it to be installed in various flow facilities and the calibration setups described in Section III.

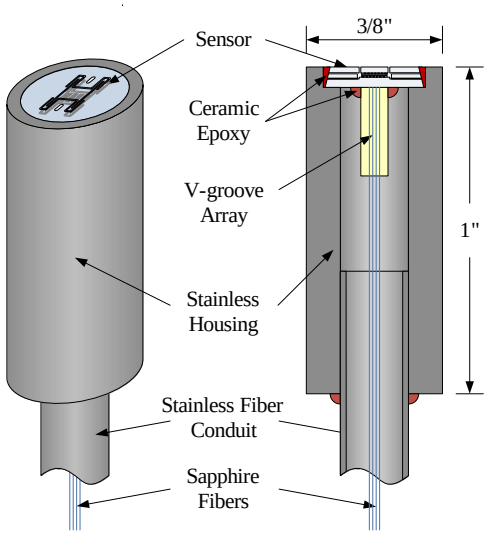

Figure 7. Illustration of the stainless steel shear stress sensor package designed for use in multiple flow facilities.

Packaging of the sensor begins by sliding the stainless steel fiber conduit and housing over the fiber array and aligning the moiré fringe segments on the sensor with the optical fibers using a custom jig fitted to Semiconductor Equipment Corp. Model 850 Flip Chip Placement System. Once the sensor and fibers are properly aligned, Cotronics 989F ceramic epoxy is applied to permanently attach the sensor and fiber array. After curing, the housing is moved into place to seat the sensor flush with the package surface and the same ceramic epoxy is used to attach the housing to the sensor and fiber conduit. The final packaged sensor is shown in Figure 8.

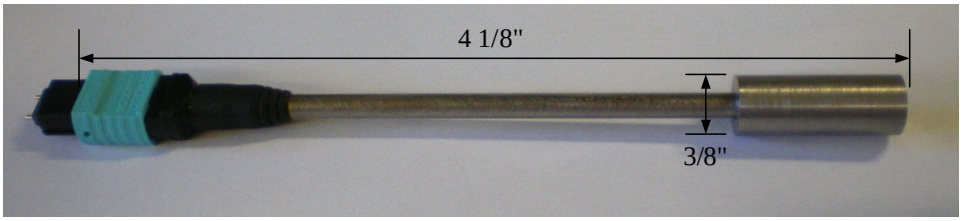

(a)

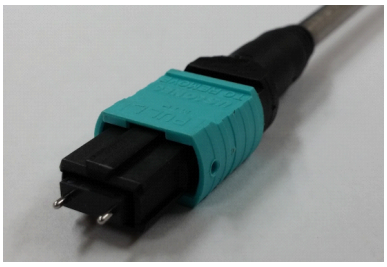

(b)

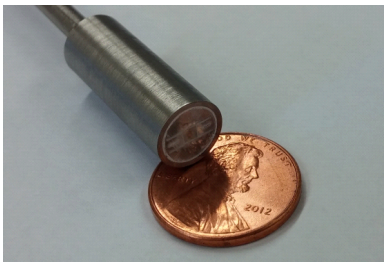

(c)

Figure 8. The packaged high-temperature shear stress sensor. (a) The overall package along with enlarged images of (b) the sapphire fiber MPO connector and (c) the packaged sensor die next to a penny.

III. Experimental Setup

The dynamic response of the sensor, including the ac wall shear stress and pressure sensitivity, are determined using the same experimental setup as that used in 28. An acoustic plane wave tube (PWT) with a $1\ in \times 1\ in$ cross-section supports the propagation of acoustic plane waves up to a cut-on frequency of $6.7\ kHz$ in air. Calibration of shear stress sensors using the Stokes-layer excitation technique first demonstrated by Sheplak et al.[33] is performed by generating a frequency-dependent wall shear stress $\tau_w(\omega)$ caused by the oscillating pressure and velocity fields created by an acoustic driver in conjunction with the no-slip boundary condition at the wall. A sound hard boundary at the termination creates a standing wave pattern, and the shear stress sensor is mounted in the side wall of the PWT at a known location such that the wall shear stress and endwall pressure p' are related by the expression[34]

$$\tau_w(\omega) = -\frac{1}{c}\sqrt{j\omega\nu}\tanh\left(a\sqrt{\frac{j\omega}{\nu}}\right)\frac{e^{jkd_s} - Re^{-jkd_s}}{1+R}p'e^{j\omega t}, \tag{9}$$

where c is the isentropic speed of sound, ν is the kinematic viscosity, a is the half height of the duct, $k = \omega/c$ is the acoustic wavenumber, d_s is the sensor distance from the boundary, and R is the measured reflection coefficient of the assumed sound hard boundary.

The wall shear stress sensitivity at a single test frequency is determined using the setup shown in Figure 9(a), with the sensor located in the side of the PWT at a pressure minimum relative to a fixed rigid termination. The acoustic source is a BMS 4590P compression driver connected to a Crown XLS1500 amplifier. The amplifier output is controlled by sending the desired frequency and voltage via a LabVIEW-controlled HP 33220A waveform generator. A $1/8''$ Brüel & Kjær (B&K) 4138 microphone is placed in the rigid termination as a pressure reference for estimating the wall shear stress at the sensor location via Equation 9. Voltages from the four outputs of the photodiode array and the reference microphone are simultaneously sampled by a National Instruments (NI) data acquisition system (DAQ) with an NI PXI-4498 card in an NI PXI-1042Q chassis. The pressure sensitivity is determined using a similar setup with the sensor placed alongside the reference microphone in the rigid termination of the PWT as shown in Figure 9(b).

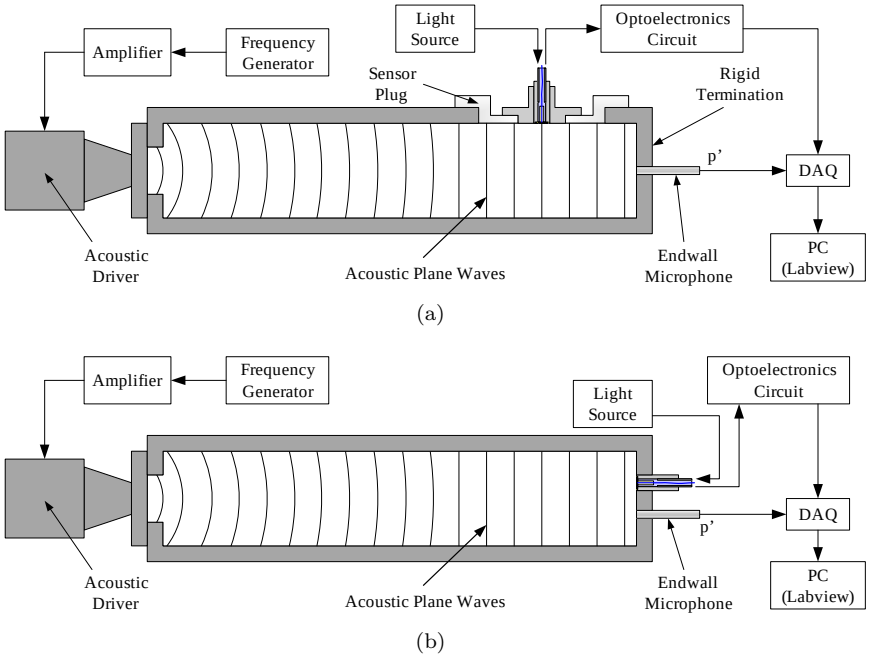

Figure 9. Illustrations of plane wave tube configurations including (a) the single frequency wall shear stress sensitivity calibration and (b) the pressure sensitivity calibration setup.

IV. Experimental Results

IV.A. Dynamic Shear Stress Sensitivity

The shear stress sensitivity calibration is performed at a test frequency of 1128 Hz, based on the sensor location in the side wall of the PWT 3 in from the rigid termination. The waveform generator output is adjusted using the secant method to achieve the desired sound pressure level (SPL) and thus wall shear stress prior to sensor data acquisition by recording the reference microphone voltage. Because the experimental data is ac coupled, determination of the moiré fringe phase using the quadrature technique cannot be performed without adding a dc offset to each of the voltage signals. This offset is a function of the amount of light coupled from the source to sensor as well as the location of the fiber on the moiré fringe pattern. Because of the difficulty in accurately determining the locations of the fibers on the fringe pattern, the ac shear stress sensitivity of the individual channels is used as the offset as previously done by Mills et al.[28] A linear fit to the voltage data for shear stress values with coherence >0.95 is performed to determine the sensitivity of each channel after which each sensitivity is normalized to that of channel one. The normalized, offset data is then used to estimate the phase of the moiré fringe.

During initial calibrations a poor response was observed from two of the sensor channels which severely reduce the effectiveness of the quadrature phase estimation method; therefore, the differential voltage sensitivity was determined using only channels 1 and 3, the results of which are shown in Figure 10. The major contributors to the error estimates in the wall shear stress and differential voltage are uncertainties in the measured pressure and normalized rms error in the autospectral density, respectively. A linear fit was performed to the data for shear stress values $\geq$10.1 mPa, yielding an estimated sensitivity of 76.8 $\mu V/Pa$ at 1.128 kHz.

IV.B. Dynamic Pressure Sensitivity

Although both the quadrature moiré fringe phase estimation technique and the differential voltage measurement used reduce pressure sensitivity, in practice some response to pressure is expected due to manufacturing defects and other irregularities. Figure 11 shows the resulting differential voltage measurement using the scaling factors determined during dynamic shear stress sensitivity calibration at a test frequency of 1128 Hz. It is believed that the reduced response at 155 and 160 dB is due to damage sustained by one of the folded tethers during the test which led to an asymmetric out-of-plane displacement. Performing a fit to

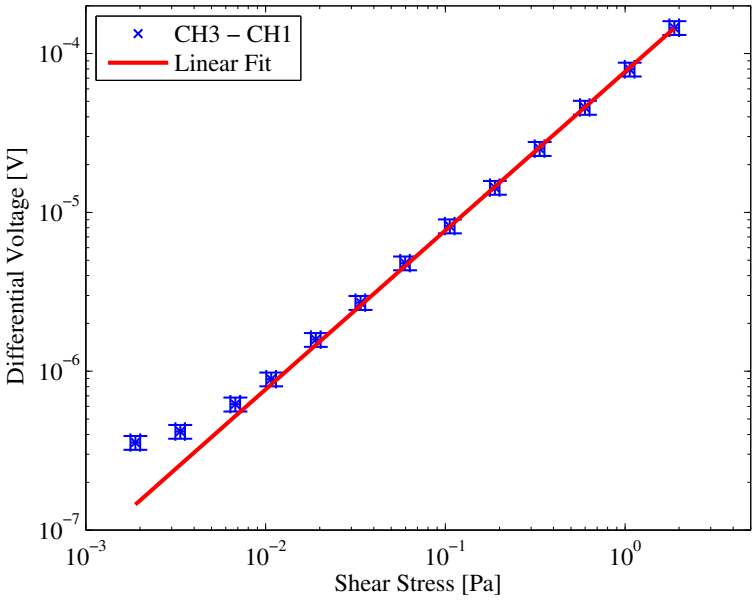

Figure 10. Dynamic sensitivity of the shear stress sensor during dynamic calibration with a fixed sound hard termination.

the data for SPLs between 130 dB and 150 dB where the response is linear yields a pressure sensitivity estimate of 13.8 nV/Pa. Comparison of the pressure sensitivity S_p with the shear stress sensitivity S from the single-frequency dynamic calibration yields a pressure rejection ratio H_p of 75 dB, computed using the expression

$$H_p = 20 \log \left(\frac{S}{S_p} \right). \tag{10}$$

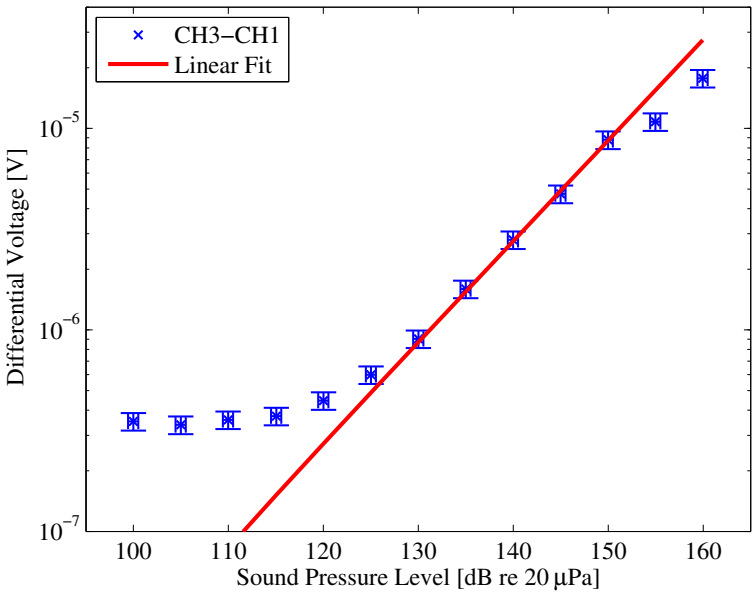

Figure 11. Pressure sensitivity of the shear stress sensor during dynamic calibration with a fixed sound hard termination.

V. Conclusion

The direct, time-resolved measurement of wall shear stress in high-temperature, high-speed flows and other harsh environments is an important measurement capability for improving the understanding of the complex flow fields associated with these environments. In the previous sections, the design, packaging, and characterization of the first sapphire micromachined wall shear stress sensor were presented. Use of geometric moiré optical transduction, a folded tether floating element design, and a sapphire optical fiber array within a stainless steel package enable a theoretical maximum operating temperature in excess of $800°C$. Dynamic calibration of the sensor system in differential mode resulted in a shear stress sensitivity of 76.8 $\mu V/Pa$ at 1.128 kHz, sensor resonance of 3.5 kHz, and a pressure sensitivity of 13.8 nV/Pa at 1.128 kHz. The resulting pressure rejection ratio of 75 dB provides confidence in the ability to accurately capture wall shear stress data within high speed flows where the pressure fluctuations can often be orders of magnitude larger than the shear stress fluctuations. The noise floor of 0.35 $\mu V/\sqrt{Hz}$ at 1.128 kHz for a 1 Hz bin indicates a minimum detectable shear stress of 4.6 mPa, resulting in a setup-limited experimentally verified dynamic range of 52 dB.

Future work will focus on improving the robustness of the laser machined floating elements as well as refinements to the packaging of the sensor and sapphire fiber array. In addition, calibration at higher shear stress levels and elevated temperatures will be performed to experimentally validate the sensor system over a larger operating range, followed by transition of the sensor system to a high-speed wind tunnel for additional characterization.

Acknowledgments

This work was funded in part by Air Force contracts FA9550-14-C-0060 and FA9550-09-C-0108, NASA contract NNX11CG90P, and the FAA Center of Excellence for Commercial Space Transportation. The authors would also like to thank the Nanoscale Research Facility for fabrication assistance.

References

[1]Gad-el Hak, M., "Introduction to Flow Control," *Flow Control*, edited by M. Gad-el Hak and A. Pollard, Vol. 53 of *Lecture Notes in Physics monographs*, Springer Berlin / Heidelberg, 1998, pp. 1–107.

[2]Winter, K., "An outline of the techniques available for the measurement of skin friction in turbulent boundary layers," *Progress in Aerospace Sciences*, Vol. 18, 1979, pp. 1 – 57.

[3]Haritonidis, J., *The measurement of wall shear stress*, 1989, pp. 229–261.

[4]Naughton, J. and Sheplak, M., "Modern developments in shear-stress measurement," *Progress in Aerospace Sciences*, Vol. 38, No. 6-7, 2002, pp. 515 – 570.

[5]Sheplak, M., Cattafesta, L., and Nishida, T., "MEMS shear stress sensors: promise and progress," *24th AIAA Aerodynamic Measurement Technology and Ground Testing Conference, AIAA 2004-2606 (invited)*, Portland, OR, June 2004.

[6]Schmidt, M., Howe, R., Senturia, S., and Haritonidis, J., "Design and calibration of a microfabricated floating-element shear-stress sensor," *Electron Devices, IEEE Transactions on*, Vol. 35, No. 6, jun 1988, pp. 750–757.

[7]Pan, T., Garverick, S., Hyman, D., Mehregany, M., and Reshotko, E., "Microfabricated Shear Stress Sensors, Part 1: Design and Fabrication," *AIAA Journal*, Vol. 37, Jan. 1999, pp. 66–72.

[8]Hyman, D., Pan, T., Reshotko, E., and Mehregany, M., "Microfabricated Shear Stress Sensors, Part 2: Testing and Calibration," *AIAA Journal*, Vol. 37, Jan. 1999, pp. 73–78.

[9]Zhe, J., Modi, V., and Farmer, K., "A microfabricated wall shear-stress sensor with capacitative sensing," *Microelectromechanical Systems, Journal of*, Vol. 14, No. 1, feb. 2005, pp. 167 – 175.

[10]Chandrasekharan, V., Sells, J., Meloy, J., Arnold, D., and Sheplak, M., "A microscale differential capacitive direct wall-shear-stress sensor," *Microelectromechanical Systems, Journal of*, Vol. 20, No. 3, june 2011, pp. 622 –635.

[11]Meloy, J., Griffin, J., Sells, J., Chandrasekharan, V., Cattafesta, L., and Sheplak, M., "Experimental verification of a MEMS based skin friction sensor for quantitative wall shear stress measurement," *41st AIAA Fluid Dynamics Conference and Exhibit*, Honolulu, Hawaii, jun 2011.

[12]Padmanabhan, A., Goldberg, H., Breuer, K., and Schmidt, M., "A wafer-bonded floating-element shear stress microsensor with optical position sensing by photodiodes," *Microelectromechanical Systems, Journal of*, Vol. 5, No. 4, dec 1996, pp. 307 –315.

[13]Horowitz, S., Chen, T., Chandrasekaran, V., Nishida, T., Cattafesta, L., and Sheplak, M., "A micromachined geometric moiré interferometric floating-element shear stress sensor," *42nd AIAA Aerospace Sciences Meeting and Exhibit, AIAA Paper 2004-1042*, Reno, NV, jan 2004, pp. 1–10.

[14]Chen, T., Mills, D., Chandrasekaran, V., Zmuda, H., and Sheplak, M., "Optical miniaturization of a MEMS-based floating element shear stress sensor with moiré amplification," *48th AIAA Aerospace Sciences Meeting, AIAA Paper 2010-0498*, jan 2010, pp. 1–13.

[15]Shajii, J., Ng, K., and Schmidt, M., "A microfabricated floating-element shear stress sensor using wafer-bonding technology," *Microelectromechanical Systems, Journal of*, Vol. 1, No. 2, jun 1992, pp. 89 –94.

[16]Goldberg, H., Breuer, K., and Schmidt, M., "A silicon wafer-bonding technology for microfabricated shears-stress sensors with backside contacts," *Solid State Sensor and Actuator Workshop*, Hilton Head, SC, 1994, pp. 111–115.

[17]Barlian, A., Park, S., Mukundan, V., and Pruitt, B., "Design and characterization of microfabricated piezoresistive floating element-based shear stress sensors," *Sensors and Actuators A: Physical*, Vol. 134, No. 1, 2007, pp. 77 – 87.

[18]Li, Y., Chandrasekharan, V., Bertolucci, B., Nishida, T., Cattafesta, L., and Sheplak, M., "A MEMS shear stress sensor for turbulence measurements," *46th AIAA Aerospace Sciences Meeting and Exhibit, AIAA-2008-269*, Reno, NV, January 2008.

[19]Kroetz, G., Eickhoff, M., and Moeller, H., "Silicon compatible materials for harsh environment sensors," *Sensors and Actuators A: Physical*, Vol. 74, No. 1-3, April 1999, pp. 182–189.

[20]Ned, A., Okojie, R., and Kurtz, A., "6H-SiC pressure sensor operation at 600 deg C," *High Temperature Electronics Conference, 1998. HITEC. 1998 Fourth International*, 1998, pp. 257–260.

[21]von Berg, J., Ziermann, R., Reichert, W., Obermeier, E., Eickhoff, M., Krötz, G., Thoma, U., Cavalloni, C., and Nendza, J., "Measurement of the cylinder pressure in combustion engines with a piezoresistive beta;-SiC-on-SOI pressure sensor," *Fourth International High Temperature Electronics Conference, 1998. HITEC.*, 1998, pp. 245–249.

[22]Tiliakos, N., Papadopoulos, G., O'Grady, A., Modi, V., Larger, R., and Frechette, L., "A MEMS-Based Shear Stress Sensor for High Temperature Applications," *46th AIAA Aerospace Sciences Meeting and Exhibit*, Reno, NV, 2008.

[23]Werner, M., Gluche, P., Adamschik, M., Kohn, E., and Fecht, H., "Review on diamond based piezoresistive sensors," *IEEE International Symposium on Industrial Electronics, 1998. Proceedings. ISIE '98.*, Vol. 1, 1998, pp. 147 –152.

[24]Zaitsev, A., Burchard, M., Meijer, J., Stephan, A., Burchard, B., Fahrner, W., and Maresch, W., "Diamond pressure and temperature sensors for high-pressure high-temperature applications," *Physica Status Solid A - Applied Research*, Vol. 185, No. 1, May 2001, pp. 59–64.

[25]Soeda, M., Kataoka, T., Ishikura, Y., Kimura, S., Masuda, T., Yoshikawa, Y., and Nagata, M., "Sapphire-based capacitive pressure sensor for high temperature and harsh environment application," *Sensors, 2002. Proceedings of IEEE*, Vol. 2, 2002, pp. 950 – 953.

[26]Ishihara, T., Sekine, M., Ishikura, Y., Kimura, S., Harada, H., Nagata, M., and Masuda, T., "Sapphire-based capacitance diaphragm gauge for high temperature applications," *Transducers '05: The 13th International Conference on Solid-State Sensors, Actuators and Microsystems*, Vol. 1, 2005, pp. 503 – 506.

[27]Mills, D., Chen, T., and Sheplak, M., "A MEMS optical moiré shear stress sensor for harsh environment applications," *Solid State Sensor, Actuator and Microsystems Workshop*, Hilton Head, SC, 2014, pp. 235–238.

[28]Mills, D., Chen, T., and Sheplak, M., "Characterization of an optical moiré wall shear stress sensor for harsh environments," *53rd AIAA Aerospace Sciences Meeting, AIAA Paper 2015-1917*, Orlando, FL, 2015.

[29]Mills, D., Blood, D., and Sheplak, M., "Development of a sapphire optical wall shear stress sensor for high-temperature applications," *Solid-State Sensors, Actuators and Microsystems (TRANSDUCERS), 2015 Transducers - 2015 18th International Conference on*, June 2015, pp. 1295–1298.

[30]Blood, D., Mills, D., Sheplak, M., and Schmitz, T., "Picosecond laser ablation of sapphire for high-temperature sensor fabrication," *Technologies for Future Micro-Nano Manufacturing Workshop*, Napa, CA, 2011, pp. 222–225.

[31]Tang, W., Nguyen, T.-C., and Howe, R., "Laterally driven polysilicon resonant microstructures," *Micro Electro Mechanical Systems, 1989, Proceedings, An Investigation of Micro Structures, Sensors, Actuators, Machines and Robots. IEEE*, Feb 1989, pp. 53–59.

[32]Li, Y., Papila, M., Nishida, T., Cattafesta, L., and Sheplak, M., "Modeling and optimization of a side-implanted piezoresistive shear stress sensor," Vol. 6174, 2006, pp. 617409–617409–12.

[33]Sheplak, M., Padmanabhan, A., Schmidt, M., and Breuer, K., "Dynamic calibration of a shear stress sensor using Stokes-layer excitation," *AIAA Journal*, Vol. 39, No. 5, JUN 2001, pp. 819–823.

[34]Chandrasekharan, V., *A microscale differential capacitive direct wall shear stress sensor*, Ph.D. thesis, Department of Mechanical and Aerospace Engineering, University of Florida, 2009.